Nuclear Inst. and Methods in Physics Research, A 871 (2017) 35–41

Contents lists available at ScienceDirect

Nuclear Inst. and Methods in Physics Research, A

journal homepage: www.elsevier.com/locate/nima

Development of a solenoid spectrometer for nuclear astrophysical studies of fusion reactions near stellar energies

X. Fang [a,b,*], B. Bucher [b,c], A. Howard [b,1], J.J. Kolata [b], Y.J. Li [d], A. Roberts [b], X.D. Tang [e], M. Wiescher [b]

[a] Sino-French Institute of Nuclear Engineering and Technology, Sun Yat-Sen University, Zhuhai 519082, China
[b] Joint Institute for Nuclear Astrophysics, Department of Physics, University of Notre Dame, Notre Dame, IN 46556, USA
[c] Idaho National Laboratory, Idaho Falls, ID 83415, USA
[d] Department of Nuclear Physics, China Institute of Atomic Energy, Beijing 102413, China
[e] Institute of Modern Physics, Chinese Academy of Science, Lanzhou, Gansu 730000, China

ARTICLE INFO

Keywords:
Nucleosynthesis
Solenoid spectrometer
Magnetic field
$^{12}C(^{12}C,p)^{23}Na$
PSSD
SSNAP

ABSTRACT

A solenoid spectrometer for nuclear astrophysics (SSNAP) has been developed to study heavy-ion fusion reactions of astrophysical importance near stellar energies. Charged particles follow helical trajectories within the strong magnetic field of a superconducting solenoid. The $^{12}C(^{12}C, p)^{23}Na$ reaction was studied as the first measurement using the solenoid spectrometer at the University of Notre Dame within the energy range of $E_{c.m.}$ = 4.0 to 6.0 MeV. This experiment demonstrated that the solenoid spectrometer is able to provide outstanding capability for detection of light charged particles produced by nuclear fusion reactions having a relatively wide energy range.

© 2017 Elsevier B.V. All rights reserved.

1. Introduction

Fusion reactions involving ^{12}C and ^{16}O at low energies are of great astrophysical importance for understanding the nucleosynthesis during late stellar evolution [1]. The main challenge in experimental nuclear astrophysics is how to measure the extremely small cross sections with enough precision near Gamow peak energies. Examples of these reactions, such as $^{12}C+^{12}C$, $^{12}C+^{16}O$ and $^{16}O+^{16}O$ that characterize the carbon burning and later oxygen burning phases of massive stars ($M\geq 8M_{\odot}$), are crucial in a wide variety of stellar burning scenarios [1,2]. Carbon burning in the core of stars occurs at temperatures of T=0.6–1.0 GK, depending on the mass of the star, corresponding to center of mass energies between 1.0 and 3.5 MeV. The primary reaction channels and Q-values are $^{12}C(^{12}C,p)^{23}Na$ (Q = 2.24 MeV), $^{12}C(^{12}C,\alpha)^{20}Ne$ (Q = 4.62 MeV) and $^{12}C(^{12}C,n)^{23}Mg$ (Q = −2.60 MeV) as shown in Fig. 1. The stellar reaction rates determine the evolutionary paths of medium to massive stars and the associated nucleosynthesis. For massive stars the carbon burning rates affect the abundances of Ne, Na, Mg but impact also the production of heavier elements. It was shown that the production yields of ^{26}Al and ^{60}Fe in supernovae, two important galactic radioactive tracers, are sensitive to the carbon fusion rate [3]. The carbon fusion reaction is also considered to be responsible for igniting the explosions in type Ia supernovae [1]. Type Ia supernovae, as "standard candles", are often used to measure precise distances of galaxies. In the late 1990s, distance measurements based on type Ia supernovae revealed that the universe expansion is accelerating [4,5]. However, it has been discovered that Type Ia supernovae that were considered the same are in fact different. A more precise study of the formation mechanism for Type Ia supernovae could lead to a re-estimation of the expansion rate of the universe and the weight of dark energy.

Due to the exponentially decreasing cross section towards lower energies, precise experimental data of $^{12}C+^{12}C$ fusion is difficult to obtain at energies within the Gamow window. Therefore, the reaction rates rely on a number of extrapolations based on different model assumptions from reaction and structure theory. Not surprisingly, there are large discrepancies between the various model extrapolations. Traditionally, the optical model is used to fit the experimental data at higher energies and then predict the cross section values at the lower energies [2]. Recently, the hindrance model was proposed, introducing an additional term in the barrier potential [6]. This translates into a significant reduction of the cross sections towards lower energies. Moreover, strong narrow resonance structures were observed for the

* Corresponding author at: Sino-French Institute of Nuclear Engineering and Technology, Sun Yat-Sen University, Zhuhai 519082, China.
E-mail address: fangx26@mail.sysu.edu.cn (X. Fang).
[1] Current address: Heinz Maier-Leibnitz Zentrum (MLZ), FRM-II, Technische Universität München, D-85748 Garching, Germany.

http://dx.doi.org/10.1016/j.nima.2017.07.050
Received 17 June 2017; Received in revised form 16 July 2017; Accepted 24 July 2017
Available online 29 July 2017
0168-9002/© 2017 Elsevier B.V. All rights reserved.

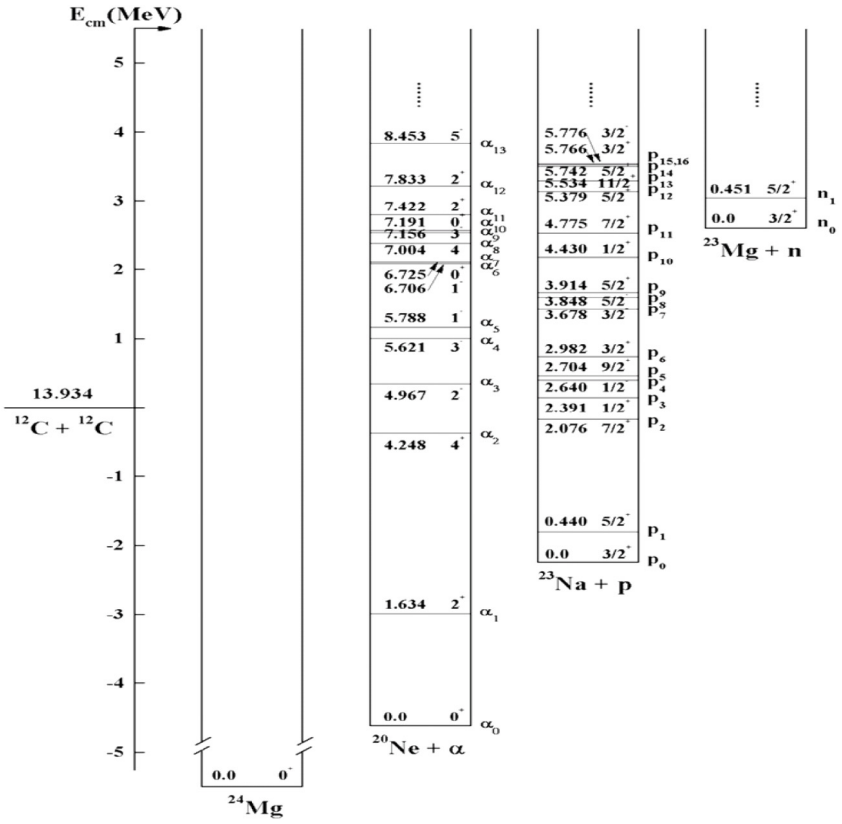

Fig. 1. The primary reaction channels of $^{12}C+^{12}C$ fusion. p_i and α_i represent the protons produced with ^{23}Na and α produced with ^{20}Ne at the ith excited state $i = 0, 1, 2, 3 \ldots$.

$^{12}C+^{12}C$ cross sections at sub-barrier energies. The existence of such resonances in the Gamow window could substantially enhance the carbon burning reaction rate [7]. To remove these discrepancies and uncertainties in the theoretical predictions, measurements that can provide more precise data need to be extended to stellar energies.

The direct measurements of the emitted charged particles and γ rays are applied to provide reliable cross section values. For the direct measurement of $^{12}C+^{12}C$, due to the extremely small cross sections (~nb), particle-γ ray coincidence methods are usually used to eliminate background. However, residual nuclei in their ground states cannot be identified by coincidence methods because there are no γ rays emitted from them [8]. The importance of these nuclei is obvious, e.g. the weight of the ^{23}Na ground state is about 30%–60% for the $^{12}C(^{12}C,p)^{23}Na$ reaction at E_{cm} = 1.0–3.0 MeV. Therefore, a new method to collect light charged particles from fusion reactions at astrophysical energies has been proposed and proven to be efficient in this article. The solenoid spectrometer for nuclear astrophysics, uses the *TwinSol* solenoid system [9] at the University of Notre Dame to supply strong magnetic fields (up to 6 T). This new experimental method can measure fusion reactions near stellar energies with relatively high efficiency through a simple detection setup. It is demonstrated that the strong magnetic field of such an instrument greatly reduces background from free electrons and multiple scattered beam particles. The $^{12}C(^{12}C,p)^{23}Na$ reaction is the first measurement using the solenoid spectrometer.

2. Experimental procedure

2.1. The concept

The solenoid spectrometer of the Nuclear Science Laboratory(NSL) at the University of Notre Dame was inspired by the first helical orbit spectrometer in the world, HELIOS at Argonne National Laboratory. The detailed concept is described in Ref. [10]. HELIOS was built and demonstrated powerful abilities of investigating reactions in inverse kinematics. We have been building a similar spectrometer using the existing *TwinSol* system at NSL [9]. The solenoid spectrometer is based on the concept that charged particles undergo helical motion resulting from the Lorentz force in a uniform magnetic field. To realize this concept, the target and silicon detectors are both placed along the solenoid axis in the field. Thus, the charged particles emitted from the target move along helical orbits, and are then bent back and collected by position sensitive silicon detectors oriented along the solenoid axis. All particles with orbits not exceeding the solenoid chamber inner radius will consequently return to the axis. A schematic drawing of the proposed spectrometer is shown in Fig. 2. It shows the recoil measurement setup that covers backward with a large solid angle, and it can be easily converted to another setup by placing the silicon detectors at forward. The silicon detectors measure the particle's energy, distance from the target, and time of flight (TOF). With the energy and target-to-detector distance information, it is possible to reconstruct the emitted angles and the excitation energies of the coupled reaction residuals. Compared to the traditional detection method, the solenoid spectrometer could provide much better energy resolution and a larger solid angle, resulting in high-detection efficiency and excellent particle identification. A proof-of-principle measurement of the $^{12}C+^{12}C$ fusion reaction was performed at energies E_{cm} = 4.0, 5.0 and 6.0 MeV, detecting protons and α particles from the $^{12}C(^{12}C,p)^{23}Na$ and $^{12}C(^{12}C,\alpha)^{20}Ne$.

2.2. The setup for the first measurement with solenoid spectrometer

The core part of the solenoid spectrometer is the superconducting solenoid, which is liquid-helium cooled, that provides magnetic fields. Each solenoid of *TwinSol* includes a 30 cm bore with the capability of producing central fields up to 6 T in strength. The NbTi coil of each solenoid is 60 cm long with an inner radius of 17.8 cm and an outer radius of 20.4 cm. To investigate the non-uniformity of the field, the field map was calculated and shown in Fig. 3. The radial symmetry is

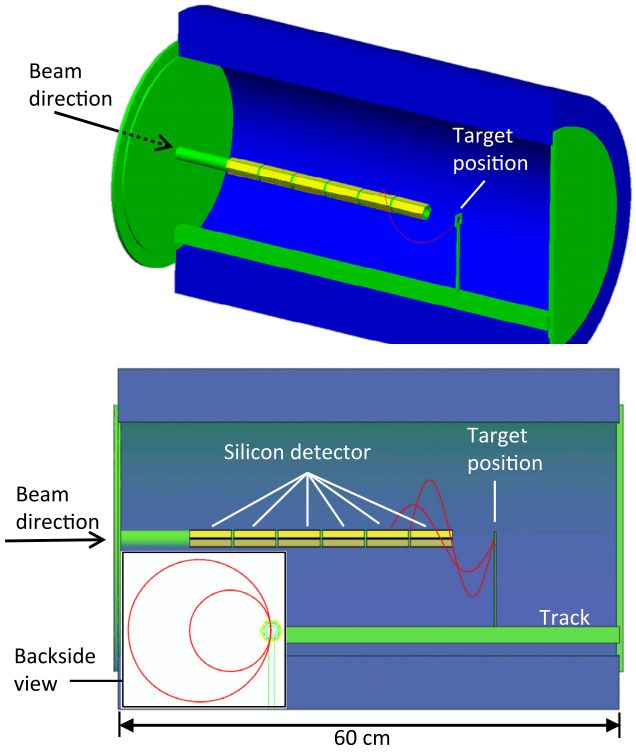

Fig. 2. The schematic of the designed solenoid spectrometer. The beam particles travel from left to right through the hollow tube along the axis of the solenoid and hit the target, the position of which is adjustable along a track. The reaction products (red spiral) at backward angles are emitted and bent back to the axis after one cyclotron period; the left-bottom small figure shows the backside view. The position-sensitive silicon detector array (yellow segments), with a total length of 31 cm and a radius of 1.2 cm located around the axis, records energy, distance between target position and particle detected position, and the TOF with respect to beam pulses.

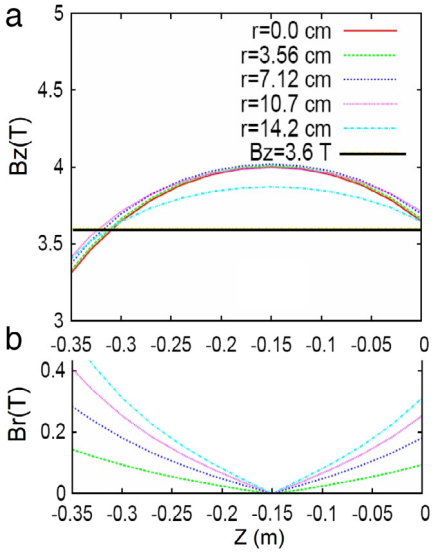

Fig. 3. Calculated map of the axial component (Bz) and the radial component (Br) of the magnetic field inside of solenoid at several radial distances r = 0.0, 3.56, 7.12, 10.7, 14.2 cm. The central field is set to be 4.0 T. The center of the field is shifted to the position of z = −0.15 m. The target is located at the origin while the detector array covers the range from z = −0.05 m to z = −0.35 m. The horizontal line in the plot (a) corresponds to 90% of the central axial field value. Through the entire range, the change of the radial component is less than 10% of the central magnetic field.

better than 10^{-4}. The field non-uniformities along the solenoid field axis were investigated through Monte Carlo simulations. The results are shown in Fig. 6 (bottom).

Fig. 4 presents the experimental setup of the solenoid spectrometer. A 20 μg/cm^2 thick graphite foil was placed at an adjustable location around the center of the solenoid, as the target. Two one-dimensional position sensitive silicon detectors(PSSD) were mounted onto the surface of a one-inch diameter aluminum tube along the field axis in the upstream direction with respect to the target. Each silicon detector was of 5 cm × 1 cm size. The distance between the nearest edge of silicon detector and the target was arranged as 8 cm in the test measurement. Two 5 mm-diameter circular collimators were installed at upstream and downstream positions respective to the target for improving the beam-tuning. The detection setup was contained within the second solenoid. Meanwhile, the focusing capability of the first solenoid was used for improving the beam optics and minimizing the size of the beam-spot on target.

The energy signals from the silicon detector were processed by *Canberra* 203 T pre-amplifiers followed by an *Ortec* 572 amplifier. The shaping time of the amplifier was set to be 3 μs to fully collect the charges from the particle-induced ionization in the silicon detectors. The four position signals were fed into a 8-channel *Mesytec* preamplifier followed by a 16-channel *Mesytec* amplifier. The shaping time of the amplifier was set to be 2 μs. Initially, the magnetic field of the solenoid was brought up step-by-step by increasing the current, while the performance of the solenoid spectrometer was evaluated using an ^{241}Am-^{148}Gd mixed α-source at the target position. The energy resolution was 54 keV (FWHM) for 5.486 MeV α particles. The position resolution was about 1 mm (FWHM).

2.3. The ^{12}C(^{12}C, p)^{23}Na measurement

The performance of the solenoid spectrometer was tested using the ^{12}C(^{12}C, p)^{23}Na and ^{12}C(^{12}C, α)^{20}Ne reactions in the energy range of E_{cm} = 4.0 MeV to 6.0 MeV using a ^{12}C beam from the FN tandem accelerator at the University of Notre Dame. The primary reaction channels of the ^{12}C+^{12}C fusion are shown in Fig. 1. The magnetic field was set to be 4.0 T for all measurements. The first spectrum recorded by the solenoid spectrometer, measured at E_{cm} = 6.0 MeV, is shown in Fig. 5. By comparing the first solenoid spectrometer spectrum with the prediction, which are the dashed lines calculated using Eq. (1), we have identified several types of events corresponding to the protons and α particles produced with excited states of ^{23}Na and ^{20}Ne, e.g. α_3, α_4, α_5 and α_6, p_7, $p_{8,9}$, p_{10} and p_{11}. Besides those proton and α lines, there are several low-energy wide bands with intensities that are much stronger than the proton and α particles. These background signals are suspected to be multiple-scattered ^{12}C from the upstream setup. Thus, the quality of the measurement required improvements.

To remove the background and avoid the overlapping between the protons and α particles, Mylar and aluminum foils were placed in front of the PSSDs to absorb the scattered ^{12}C beam particles and α particles from ^{12}C(^{12}C, α)^{20}Ne. This helped to achieve clean spectra for measurement at beam energies E_{cm} = 4.0, 5.0 and 6.0 MeV. The $E-(-z)$ spectrum measured at E_{cm} = 5.0 MeV is shown in Fig. 6 (top). It shows the combination of measurements with two different target locations. The detector array covers a distance of 10 cm. To cover a longer range, the measurement was done by placing the target at two different locations. The covered distance from the target is between −0.08 m and −0.18 m for the first location and between −0.24 m and −0.34 m for the second location. A 5.4 μm thick Mylar degrader was used at the first location. It was replaced by a 5.7−μm Aluminum foil at the second location. Because of the energy loss in the degrader, the correlation between energy (E) and position ($-z$) deviates from the predicted straight lines, especially at larger distance from the detectors.

2.4. The simulation

The simulation of the detector performance is an important aspect for experiments. To address the influence of the strong magnetic field,

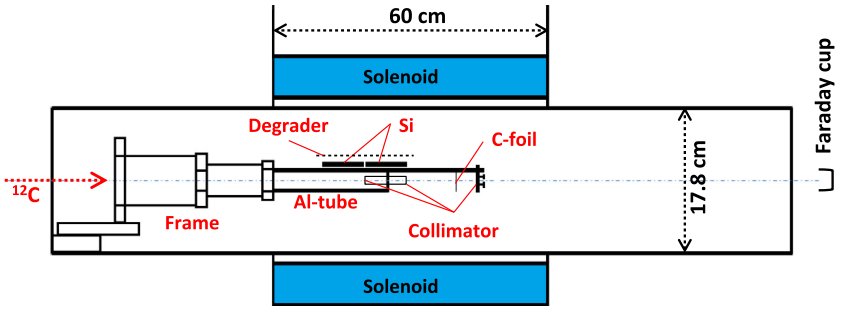

Fig. 4. The schematic of the solenoid spectrometer setup for the first measurement of ^{12}C(^{12}C, p)^{23}Na. Three collimators with 3 mm diameters were used to guarantee excellent beam alignment. The first collimator consisting of four segments provided the beam position information.

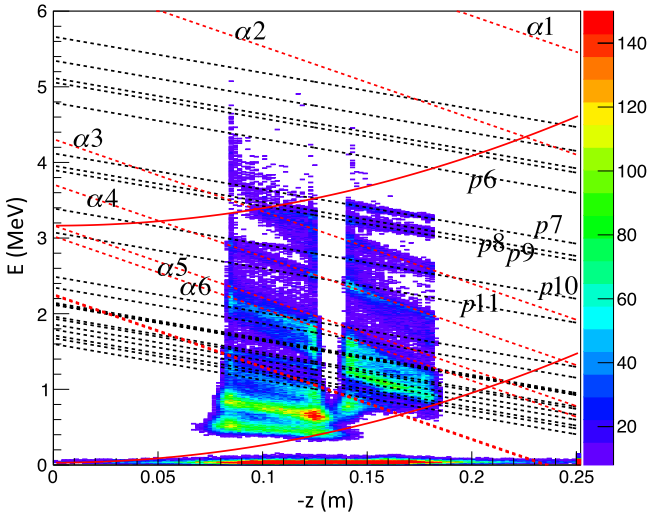

Fig. 5. The energy (E) vs. position ($-z$) spectrum measured at E_{cm} = 6.0 MeV. The target position along the solenoid axis was defined as z = 0. In this work all particles were measured at backward angles, thus the x-axis title name is '$-z$'. The predicted lines corresponding to the excited states in ^{23}Na and ^{20}Ne are shown in black and red dashed lines, respectively. To match the observation, the magnetic field used in the prediction was set as 4.4 T, 10% higher than the actual field, to compensate the effect incurred by the half inch distance of the detectors with respect to the solenoid center. The region between the two solid red curves shows the acceptance of detecting protons for a given magnetic field within the solenoid chamber inner radius [10].

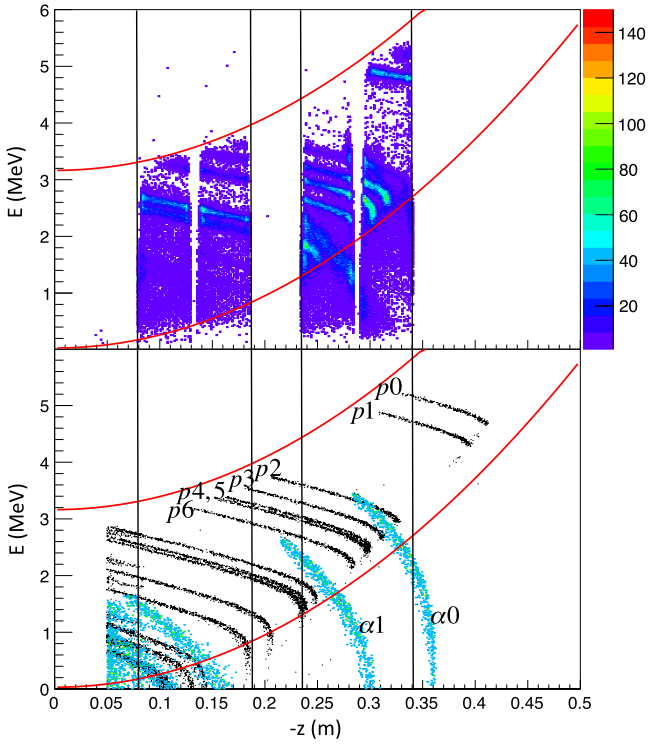

Fig. 6. (top) The energy (E) vs. position ($-z$) spectrum measured at E_{cm} = 5.0 MeV. (bottom) Simulation using GEANT4. The region between the two solid red curves highlights the acceptance of detecting protons and α particles produced from ^{12}C+^{12}C based on the experimental magnetic field and solenoid chamber inner radius. The α particles fall out of the acceptance because of their non-negligible energy loss through the degrader placed before the silicon detectors.

the sensitivity to detector position and field inhomogeneities, a Monte Carlo simulation code using $GEANT4$ was developed for the present work. First, a constant 4 T magnetic field is used in the simulation. The predicted lines for various excited states are calculated using the following equation,

$$E_a = \left(\frac{E_{beam}}{2} + Q_0 - E_x\right) \times \frac{24 - m_a}{24} - \frac{1}{2} m_a V_{cm}^2 + \left(\frac{m_a V_{cm}}{T_{cyc}}\right) z \qquad (1)$$

where E_{beam} is the incident ^{12}C beam energy; Q_0 is the reaction Q-value for the channel decaying to the ground states and is equal to 2.24 MeV for ^{12}C(^{12}C, p)^{23}Na and 4.617 MeV for ^{12}C(^{12}C, α)^{20}Ne, respectively; E_x is the excitation energy for the fusion residuals, e.g.^{23}Na,^{20}Ne; m_a is the mass number in amu for the detected light particle (1 for proton, and 4 for α); V_{cm} is the speed in the center of mass reference frame; z is the position at which the light particle is detected by the detectors, where z = 0 is the target position; T_{cyc} is the cyclotron period for the detected light particle which can be calculated using the following equation,

$$T_{cyc} = 65.6 \times \frac{m_a}{Bq}\ (ns) \qquad (2)$$

where m_a is the mass number in amu, B is the magnetic field in Tesla and q is the ion charge in unit of e. It was found that the detected protons and α particles took shorter flight times than the calculated T_{cyc}, due to the added distance between detectors and the solenoid axis (see Fig. 2). To match the simulation, the magnetic field used in the prediction are increased by 10% to compensate for the shorter flight times.

The simulated energy (E) vs. position ($-z$) spectrum using $GEANT4$ is shown in Fig. 6 (bottom). The coverage of detector is marked by two red lines. The α lines, shown in black wide bands, correspond to the α_0, α_1 and α_2. The proton lines, shown in black narrow bands, correspond to p_0, p_1, p_2, p_3, $p_{4,5}$, p_6, p_7, $p_{8,9}$, p_{10} and $p_{11,12}$. The proton lines under α_2 are not observed in the experiment due to their low energies. Comparing with the results in Fig. 6 (top), the simulation matches very well with the present measurement.

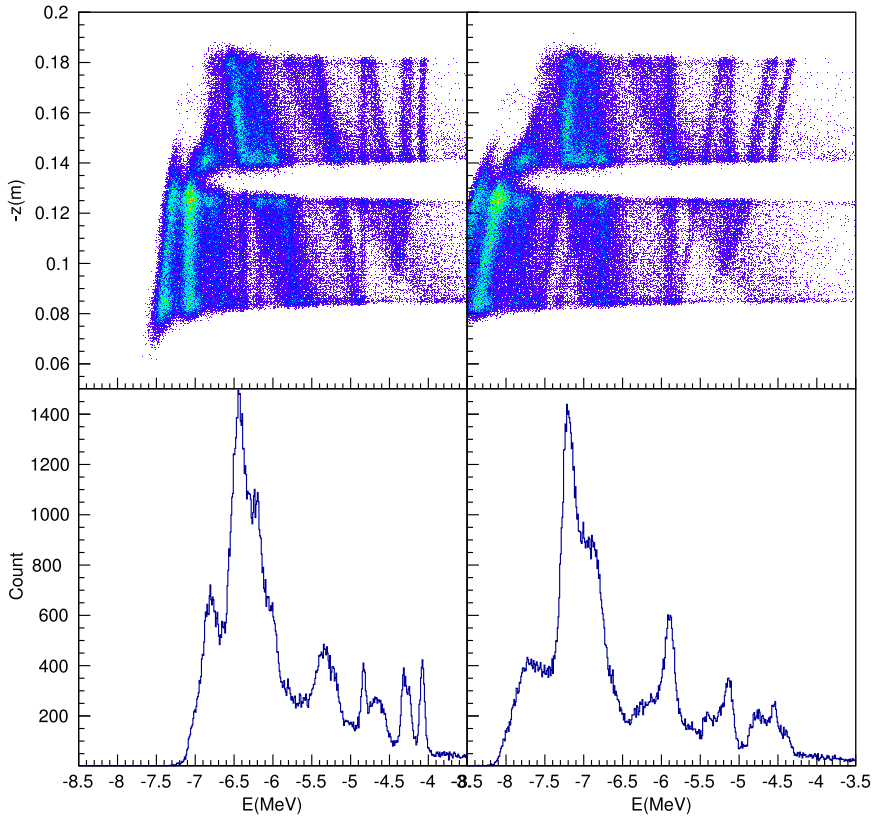

Fig. 7. The reconstructed Q-value spectra for the p+^{23}Na and the $\alpha + {}^{20}$Ne channels at $E_{\mathrm{cm}} = 6.0$ MeV. (a) The position $(-z)$ vs. Q-values (E) of the p+^{23}Na. (b) The position $(-z)$ vs. Q-values (E) of the $\alpha + {}^{20}$Ne. (c) is the projection of the spectrum in (a); (d) is the projection of the spectrum in (b).

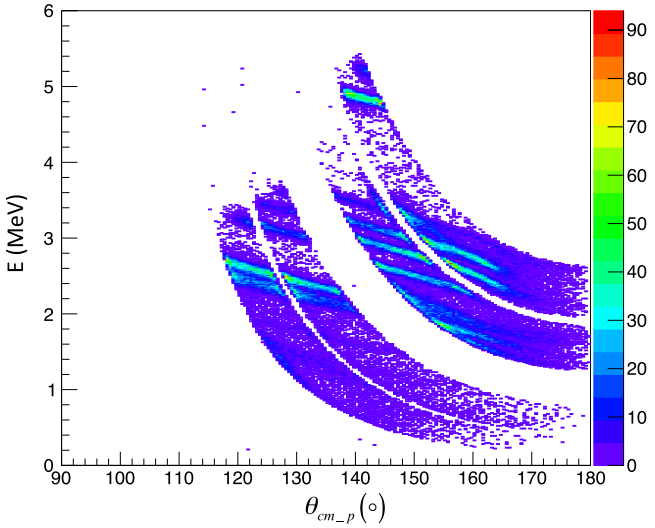

Fig. 8. The energy (E) vs. angle (θ_{cm}) spectrum measured at $E_{\mathrm{cm}} = 5.0$ MeV.

3. Results and discussion

3.1. Analysis of data without any detector shield

The present experimental data provides energy (E) and position (z) information of light charged particles (p, α). The Q-values for different excited states in ^{23}Na and ^{20}Ne are reconstructed by solving the equation Eq. (1). The corresponding spectra of Q-values are shown in Fig. 7. With the measured energies (e) and positions (z) for the protons and α particles, it is possible to determine the excited energy for the residuals, *i.e.* ^{23}Na and ^{20}Ne. The excitation energy spectrum for the p+^{23}Na channel is shown in Figs. 7(a) and (c). The excitation energy spectrum for the $\alpha + {}^{20}$Ne channel is shown in Figs. 7(b) and (d). The energy resolution for the peak corresponding to the $E_x = 3.97$ MeV state in ^{23}Na is determined as 65 keV (FWHM). The doublets (p_8 and p_9) in Fig. 7(c), $E_x = 3.85$ MeV and 3.91 MeV, are clearly separated. However, the resolution for the α peaks, which correspond to the $E_x = 4.24$ MeV and $E_x = 4.97$ MeV states in ^{20}Ne, are 120 keV; much worse than the resolution of the protons. With the detected α particle energy varying between 2.0 and 4.0 MeV, this poorer resolution mainly results from the energy loss of α particles in the target, and the effect of dead layer of the silicon detectors is only a minor factor.

3.2. Analysis of data with detector shield

To achieve clean proton spectra, a detector shield was applied to eliminate the scattered ^{12}C beam and α particles. Nevertheless, protons would lose energy when going through the shield foil. To correct the energy loss in the foil, the angle θ_{lab} is reconstructed from the detected energy (E) and position (z) information using the equation,

$$cos(\theta_{lab}) = \frac{z}{T_{cyc}}\sqrt{\frac{m}{2E}} \tag{3}$$

where T_{cyc} is the cyclotron period for protons, θ_{lab} is the emitted angle of protons with respect to the beam incident direction. With the θ_{lab} values, the corresponding effective thickness of foil is obtained from the actual thickness divided by the angle correction factor, $\sin(\theta_{lab})$. Then the proton energy could be corrected by summing the detected energy with the energy loss in the foil. The energy (E) vs. angle (θ_{cm}) of protons at $E_{\mathrm{cm}} = 5.0$ MeV is shown in Fig. 8. It is still a combination of two measurements with different target locations. A broad angle coverage from 120° to 165° is observed with the present simple setup.

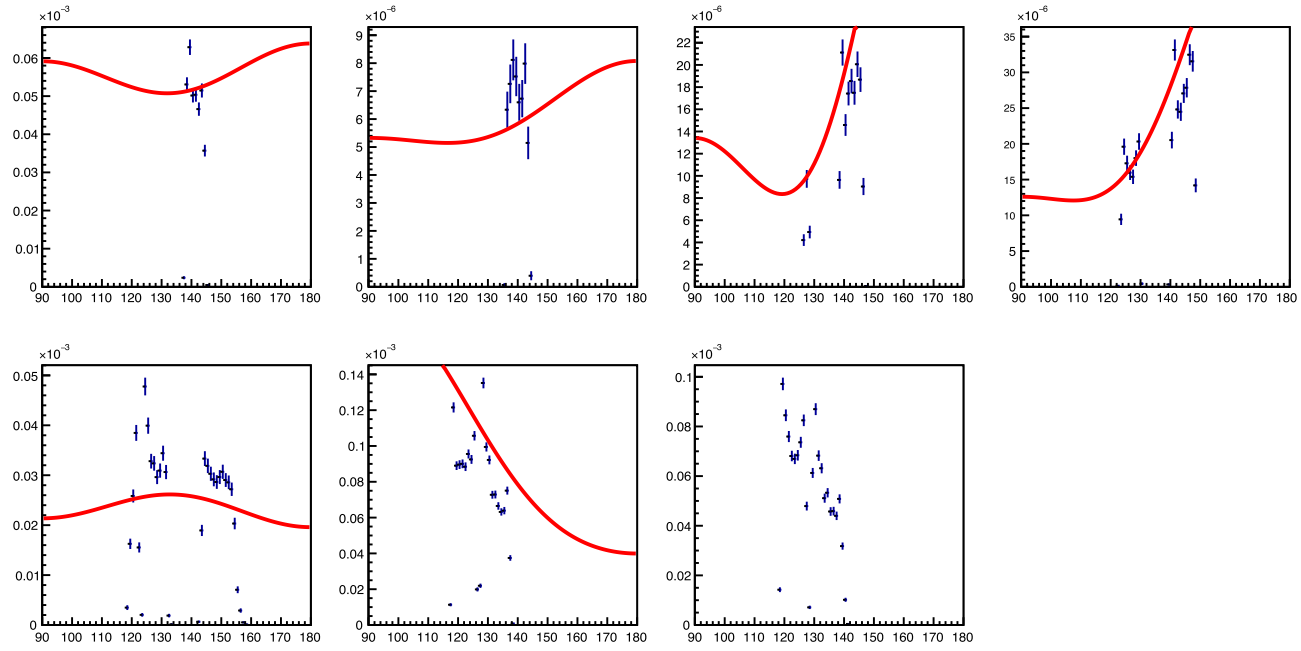

Fig. 9. The angular distribution ($d\sigma/d\Omega$ vs. θ_{cm}) spectrum of different proton peaks measured at E_{cm} = 5.0 MeV. The red curves are the angular distribution fit results from a previous measurement [8].

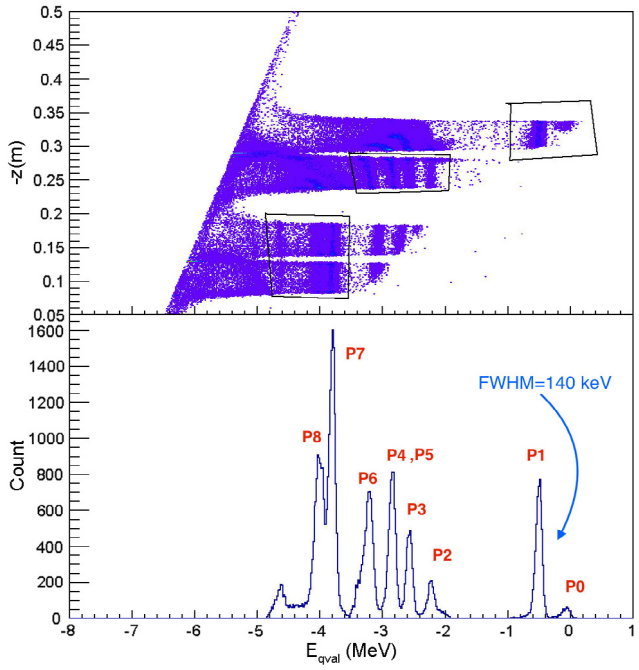

Fig. 10. The position ($-z$) vs. Q-values (E_{qval}) spectrum measured at E_{cm} = 5.0 MeV (top). Three regions (in black boxes) including some identified proton lines are chosen to provide the projection (bottom). The FWHM of p_1 peak is about 140 keV.

The angular resolution varies with protons' energies and angles, and the averaged angular resolution of proton is about 0.2°. Fig. 9 shows the angular distributions of separated proton groups, which are labeled. The red curves are the angular distribution fit results from a previous measurement, which was carried out using a large area strip silicon detector array [8]. Due to the non-linear position response at the edge of detector, there is a distortion in the measured angular distributions. Further simulation and calculation are required in future to study this non-linear effect and provide more reliable angular information.

The position ($-z$) vs. Q-values (E_{qval}) spectrum measured at E_{cm} = 5.0 MeV is shown in Fig. 10 (top). A cut is applied to the $-z$ vs. E_{qval} spectrum in Fig. 10 to select a subset of events to generate the clear projection of proton peaks. The identified peaks are labeled.

4. Summary

This work demonstrated that the solenoid spectrometer is able to provide outstanding capability to study nuclear fusion reactions for a relatively wide energy range through the measurement of charge-particle channels from $^{12}C+^{12}C$ fusion, especially the $^{12}C(^{12}C, p)^{23}Na$ reaction. Both good energy resolution (140 keV for p_1) and angular resolution (~0.2°) were achieved from the simple setup described. The solenoid spectrometer can be applied to a broad variety of sub-Coulomb barrier nuclear reactions with substantially larger efficiency than traditional detection methods. This project is being pursued further by the development of an extended silicon detection array along the solenoid axis. Upgrades were recently applied to *TwinSol*, including a multi-cell gas target and a possible third solenoid, and the final design of SSNAP is being determined [11].

Acknowledgments

This work was supported by the US National Science Foundation under Grant Nos. PHY-1419765 and PHY14-01343, the Joint Institute of Nuclear Astrophysics Center for the Evolution of the Elements grant under Grant No. PHY-1430152, the National Natural Science Foundation of China under Grant No. 11575292 and the Fundamental Research Funds for the Central Universities under Grant No. 17lgzd34.

References

[1] C.E. Rolfs, W.S. Rodney, Cauldrons in the Cosmos: Nuclear Astrophysics, University of Chicago Press, 1988.
[2] C. Iliadis, Nuclear Physics of Stars, John Wiley & Sons, 2015.
[3] M. Limongi, A. Chieffi, Nuclear Physics A 758 (2005) 11–14.
[4] A.G. Riess, A.V. Filippenko, P. Challis, A. Clocchiatti, A. Diercks, P.M. Garnavich, R.L. Gilliland, C.J. Hogan, S. Jha, R.P. Kirshner, et al., Astron. J. 116 (3) (1998) 1009.

[5] S. Perlmutter, G. Aldering, G. Goldhaber, R.A. Knop, P. Nugent, P.G. Castro, S. Deustua, S. Fabbro, A. Goobar, D.E. Groom, et al., Astrophys. J. 517 (2) (1999) 565.
[6] C.L. Jiang, K.E. Rehm, B.B. Back, R.V.F. Janssens, Phys. Rev. C 75 (2007) 015803.
[7] R.L. Cooper, A.W. Steiner, E.F. Brown, Astrophys. J. 702 (2009) 660–671.
[8] X. Fang, B. Bucher, S. Almaraz-Calderon, A. Alongi, A.D. Ayangeakaa, A. Best, G.P.A. Berg, C. Cahillane, E. Dahlstrom, M. Freer, et al., Journal of Physics: Conference Series, IOP Publishing, 2013, p. 012151.
[9] J.J. Kolata, A. Morsad, X.J. Kong, R.E. Warner, Nucl. Instr. and Meth. B 40–41 (1989) 503–506.
[10] A.H. Wuosmaa, J.P. Schiffer, B.B. Back, C.J. Lister, K.E. Rehm, Nucl. Instr. and Meth. A 580 (2007) 1290–1300.
[11] P.D. O'Malley, D.W. Bardayan, J.J. Kolata, M.R. Hall, O. Hall, J. Allen, F. Becchetti, Nucl. Instr. and Meth. B 376 (2016) 417–419.